

The stochastic X-ray variability of the accreting millisecond pulsar IGR J17062–6143

PETER BULT  ^{1,2}

¹ Department of Astronomy, University of Maryland, College Park, MD 20742, USA

² Astrophysics Science Division, NASA Goddard Space Flight Center, Greenbelt, MD 20771, USA

ABSTRACT

This work presents an investigation of the stochastic X-ray variability from the 164 Hz accreting millisecond pulsar IGR J17062–6143, based on regular observations collected with the Neutron Star Interior Composition Explorer between 2017 July and 2020 August. Over this period, the power density spectrum showed a stable morphology, with broad $\sim 25\%$ rms band-limited noise below 16 Hz. Quasi-periodic oscillations (QPOs) were occasionally observed, with the most notably detections including a low-frequency QPO centered at 2.7 Hz and a sharp QPO centered at 115 Hz that may be a 2:3 resonance with the spin frequency. Further, the energy dependence of the band-limited noise is studied through a spectroscopic analysis of the complex covariance in two frequency intervals. It is found that the power law continuum is the primary driver for the observed variability, although the thermal (blackbody) emission also appears to be intrinsically variable in area (5% rms) and temperature (1% rms). Notably, the 1 keV emission feature seen in all X-ray spectra of IGR J17062–6143 varies with the same amplitude as the power law, but systematically lags behind that continuum emission. These results appear consistent with a scenario in which a time variable Compton-scattering corona is the primary source for the observed stochastic variability, with the variability observed in the emission feature and at the lowest photon energies being due to the disk reflection of the power law continuum.

Keywords: stars: neutron – X-rays: binaries – X-rays: individual (IGR J17062–6143)

1. INTRODUCTION

Accreting millisecond X-ray pulsars (AMXPs) are rapidly rotating neutron stars that accrete matter from a low-mass binary companion star (see Di Salvo & Sanna 2020, for a recent review). These objects are characterized by their coherent pulsations; a nearly sinusoidal modulation of the X-ray emission that directly tracks the neutron star rotation. Through the study of these pulsations one can extract information on neutron star properties, such as mass, radius, or magnetic field strength (Poutanen & Gierliński 2003; Leahy et al. 2008; Psaltis et al. 2014). Additionally, pulsations can be used to study the torque exchange between the neutron star and the accretion disk (Bildsten 1998; Psaltis & Chakrabarty 1999), and investigate the evolution of the stellar binary (Nelson & Rappaport 2003).

While the pulsar properties of AMXPs alone make them interesting targets for study, these systems generally also exhibit the phenomenology seen in non-pulsating low-mass X-ray binaries (LMXBs), including accretion rate dependent state transitions (van Straaten et al. 2005), quasi-periodic variability (QPOs) (Wijnands & van der Klis 1998; van Straaten et al. 2005), and thermonuclear X-ray bursts (in 't Zand et al. 1999; Chakrabarty et al. 2003). Through this combination of pulsar and LMXB properties the different observ-

ables of AMXPs offer complementary views of the same underlying accretion processes (Wijnands et al. 2003; Chakrabarty et al. 2003; Bult & van der Klis 2015a; Bult et al. 2017).

The X-ray transient IGR J17062–6143 (simply IGR J17062 henceforth) is an especially interesting system for testing our understanding of accretion onto a weakly magnetized neutron star. The source was first discovered in Jan/Feb of 2007 (Churazov et al. 2007) and has since remained visible at a comparatively low luminosity of $L_X \approx 5 \times 10^{35}$ erg s⁻¹ (Degenaar et al. 2017; van den Eijnden et al. 2018; Bult et al. 2021a). During this unusually long outburst, IGR J17062 has shown three energetic intermediate duration type I X-ray bursts (Degenaar et al. 2013; Negoro et al. 2015; Nishida et al. 2020), but has otherwise remained remarkably stable. Previous studies have investigated its type I X-ray bursts and their interactions with the accretion environment (Degenaar et al. 2013; Keek et al. 2017; Bult et al. 2021b), the X-ray spectroscopy (Degenaar et al. 2017; van den Eijnden et al. 2018), the optical emission (Hernández Santisteban et al. 2019), and the pulsar properties and accretion torques (Strohmayer et al. 2018; Bult et al. 2021a). One aspect of this source that has so far not yet been covered, is its aperiodic variability. The current paper aims to rectify this situ-

ation. The following presents a timing analysis of Neutron Star Interior Composition Explorer (NICER, Gendreau & Arzoumanian 2017) observations that were collected between 2017 and 2020.

2. DATA PROCESSING

The first NICER observations of IGR J17062 were collected in 2017 August. Since then, NICER has returned to this target at various times, accumulating a total of 372 ks in unfiltered exposure by 2020 August. These data are available under the NICER program IDs 103410, 260101, 203410, 303410 and 361201, and were presented previously in the pulsar timing study of Bult et al. (2021a). Following the data cleaning procedures described by these authors, the data were filtered using NICERDAS v7a with standard screening criteria, except for relaxed constraints on the rate of reset triggers ($< 400 \text{ ct s}^{-1} \text{ det}^{-1}$) and on the rate of high energy events ($< 1.5 \text{ ct s}^{-1} \text{ det}^{-1}$ and $< 2.0 \times \text{COR_SAX}^{-0.633}$)¹). This process yielded 202 ks good time exposure. Barycentric correction were then applied to the clean data based on the Swift/UVOT position of Ricci et al. (2008) and the JPL-DE430 ephemeris (Folkner et al. 2014).

3. ANALYSIS AND RESULTS

The NICER data on IGR J17062 can be naturally grouped into distinct epochs based on their observation dates. For the purpose of this analysis, eight such epochs are identified. Table 1 lists the specifics of these epochs, giving the grouped ObsIDs with their summed exposures, mean 0.3 – 9 keV count rates, and $(0.3 - 1.5 \text{ keV})/(3 - 9 \text{ keV})$ hardness ratio.

Note that the data grouping used here is slightly different from the one used in Bult et al. (2021a). In particular, where they treat the observations in 2018 November and October separately, these data are grouped together into a single epoch here (epoch 2). Additionally, the data of epoch 7 was collected in response to an intermediate duration type I X-ray burst and shows large swings in the source intensity and energy spectrum (Bult et al. 2021b). These swings are seen in the first 4 days of monitoring, and are likely due to interactions between the X-ray burst emission and the accretion flow, which cause disk accretion to be temporarily inhibited in the aftermath of the burst. Because these observations do not sample IGR J17062 in its regular long-term state, the first five ObsIDs (totalling 15.6 ks) of this set were excluded from the present analysis.

3.1. Timing Analysis

For the aperiodic timing analysis I investigate the power density spectra for each of the eight data epochs.

First, the 0.3 – 9 keV event data were binned into a light curve at 1/8192-s time resolution and divided into 64-s duration segments. Each segment was then transformed into the Fourier domain and converted to a Leahy-normalized power density spectrum (Leahy et al. 1983) with a frequency resolution of $\approx 0.015 \text{ Hz}$ and a Nyquist frequency of 4096 Hz. The resulting power density spectra were then averaged per epoch. The Poisson noise level was estimated by averaging all powers with frequencies above 2000 Hz. In all cases the estimated noise level was consistent with the theoretically expected mean noise power of two. After subtracting the Poisson noise, the power spectra were finally renormalized to units of squared fractional rms with respect to the source count-rate.

The power spectrum of each epoch shows the same overall morphology: below 10 Hz the variability is characterized by strong band-limited noise, while above 10 Hz the power approaches the Poisson noise level and sometimes showed weak QPOs. This spectral shape is consistent with the power spectra observed from hard state neutron star LMXBs (van der Klis 2006), and identifies the source state as the (extreme) island state in “atoll” naming convention (Hasinger & van der Klis 1989). To quantify the power spectra, I model them using the multi-Lorentzian model of Belloni et al. (2002), with each Lorentzian expressed in terms of its integrated power, characteristic frequency ($\nu_{\max} = \sqrt{\nu_0^2 + (W/2)^2}$, where W and ν_0 are the full width at half maximum and centroid frequency), and quality factor ($Q = \nu_0/W$). An individual Lorentzian component is deemed significant if the ratio of its integrated power (from zero to infinity) over the lower bound 1σ uncertainty is greater than three. The best-fit parameters obtained through this modeling are listed in Table 2.

At low frequencies ($< 10 \text{ Hz}$), the band-limited noise consistently required two Lorentzian profiles to obtain a good fit. Using the neutron star naming convention (van Straaten et al. 2003, 2005; Altamirano et al. 2008), the lower frequency Lorentzian can be identified as the “break” component, and higher frequency term as the “hump” component. Epoch 8 showed an additional sharp QPO at 2.6 Hz. Following the same naming convention, this component is identified as the low-frequency (LF) QPO.

At higher frequencies ($> 10 \text{ Hz}$), the power spectral shape was less consistent across the different epochs. The four epochs with the least amount of exposure did not show any significant power at higher frequencies. The remaining epochs did show higher frequency power, mostly in the form of an additional broad noise component. Such broad high frequency noise is not uncommon in the power spectra of neutron stars, and is usually attributed to either the so-called ℓ ow or hectohertz components. The specific identification relies on observing how the characteristic frequencies of these Lorentzians change in relation to each other as a func-

¹ The COR_SAX parameter models the geomagnetic cut-off rigidity as function of the orbital position of the instrument, and is expressed in units of GeV c^{-1} .

Table 1. Data grouping

Epoch	ObsIDs	Date	Exposure (ks)	Rate (ct/s)	Hardness
1	1034100101 - 07	2017/Aug	17.8	34.6	0.068
2	1034100108 - 22	2017/Oct-Nov	28.5	38.3	0.081
3	1034100123 - 27	2018/Jan	2.1	46.1	0.062
4	2601010101 - 04	2019/Apr	27.5	44.3	0.066
5	2601010201 - 04	2019/Jul	23.6	35.2	0.061
6	2034100101 - 03	2019/Oct	16.9	46.8	0.070
7	3034100106 - 12	2020/Jun	10.3	37.4	0.055
8	3612010101 - 11	2020/Aug	60.1	37.5	0.030

NOTE—Count rates are calculated in the 0.3 – 9 keV band, while the hardness ratio is defined as 3 – 9 keV over the 0.3 – 1.5 keV band rates.

tion of source flux. Given that such evolution does not occur in IGR J17062 (at least not within the considered dataset), a precise identification is not possible. Instead I simply label these terms as “high-frequency noise” (HFN). Epoch 2 stands out for showing a possible QPO at 330 Hz. With a significance of 2.76σ , however, the feature is not formally significant. Because QPO amplitudes are expected to increase with photon energy, I reconstructed the power spectrum in the 1.5 – 9 keV band. Under this tighter energy selection, the QPO significance increases to 3σ , hence I tentatively consider it a marginal detection.

Comparing the fit parameters of the different epochs, it becomes clear that all observations except for epoch 6 have a similarly shaped band-limited noise structure. This similarity suggests that these data can be combined to improve sensitivity. Indeed, the combined power spectrum is more complex, as shown in Figure 1 and reported in the bottom entry of Table 2. In addition to the expected broad noise components and LF QPO, it showed two previously undetected sharp QPOs: one centered at 5.6 Hz, and the other at 115 Hz. While the former might be related to the harmonic structure of the LF QPO, the latter is not easily identified. The possible origins of these QPOs are discussed in Section 4.2.

3.2. RMS energy dependence

To investigate the energy dependence of the band-limited noise, I combined all data except for epoch 6 and calculated the rms energy spectrum. The 0.3–9 keV energy range was divided into 20 energy bins, such that each bin contained a roughly equal number of photons. The average power density spectrum was constructed for each energy bin and used to calculate the integrated fractional rms amplitudes between $1/16$ – 1 Hz and 1 – 16 Hz. These intervals were chosen such that they scale geometrically and can be associated (approximately) with the break and hump components identified in the energy-averaged power spectra. As shown in Figure 2, the rms of the slower variability is found to show a minimum at about 1.5 keV, and increases toward both higher and lower photon energies. The higher fre-

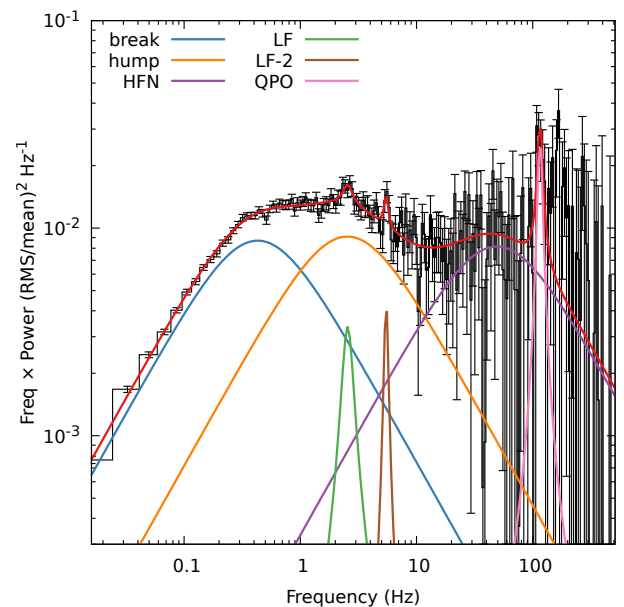


Figure 1. Averaged power density spectrum of IGR J17062 obtained by combining all data except epoch 6 (Table 1). The parameters of the best-fit model are listed in Table 2. All error bars show 1σ uncertainties.

quency interval shows a larger scatter, but appears to follow the same increasing trend below 1 keV. Above 1 keV, however, the rms increases more steeply and to a higher amplitude.

3.3. Spectral timing

A more detailed view of the joint spectral and temporal variations in the observed data can be obtained through the energy dependent cross spectrum (Uttley et al. 2014). To compute the cross spectrum, I divide the 0.3 – 9 keV energy range into 70 subject bands, each containing a roughly equal number of counts. For each subject band, a 1/128-s resolution light curve was divided into 32-s duration segments, which were subsequently transformed into the Fourier domain. Similarly,

Table 2. Power spectrum model parameters

Epoch	ID	ν_{\max} (Hz)	Quality	rms (%)	χ^2/dof
1	break	0.36 ± 0.04	0 (fixed)	14.6 ± 0.8	90 / 88
	hump	2.9 ± 0.5	0 (fixed)	18.8 ± 0.7	
2	break	0.46 ± 0.03	0 (fixed)	17.5 ± 0.6	
	hump	3.5 ± 0.3	0.33 ± 0.15	16.2 ± 1.1	66 / 92
	QPO [*]	330 ± 13	5.3 ± 2.7	14.2 ± 2.6	
3	break	0.37 ± 0.11	0.21 ± 0.16	15.7 ± 3.1	29 / 47
	hump	2.1 ± 1.3	0 (fixed)	16.0 ± 2.9	
4	break	0.43 ± 0.03	0 (fixed)	17.4 ± 0.8	
	hump	2.4 ± 0.3	0 (fixed)	18.0 ± 0.7	92/94
	HFN	40 ± 1.1	0 (fixed)	17.6 ± 2.1	
5	break	0.50 ± 0.04	0 (fixed)	16.7 ± 0.7	
	hump	3.6 ± 0.7	0 (fixed)	17.3 ± 0.9	107 / 85
	HFN	104 ± 18	0 (fixed)	32.1 ± 1.7	
6	break	0.88 ± 0.07	0 (fixed)	18.1 ± 0.8	98 / 87
	hump	6.5 ± 1.4	0 (fixed)	16.3 ± 0.9	
7	break	0.38 ± 0.04	0 (fixed)	15.4 ± 0.9	83 / 88
	hump	3.4 ± 0.6	0 (fixed)	19.1 ± 0.9	
8	break	0.42 ± 0.03	0 (fixed)	16.3 ± 0.6	
	hump	2.5 ± 0.3	0 (fixed)	17.1 ± 0.8	65 / 83
	LF	2.55 ± 0.04	7.0 ± 3.3	3.9 ± 0.8	
	HFN	43 ± 16	0 (fixed)	14.9 ± 1.5	
c	break	0.425 ± 0.015	0 (fixed)	16.5 ± 0.4	
	hump	2.5 ± 0.2	0 (fixed)	17.0 ± 0.5	
	HFN	48 ± 11	0 (fixed)	15.9 ± 1.0	168 / 186
	LF	2.57 ± 0.07	4.3 ± 2.0	3.5 ± 0.8	
	LF-2	5.56 ± 0.12	13 ± 4	2.6 ± 0.4	
	QPO	115.4 ± 2.4	7.3 ± 3.5	7.0 ± 1.3	

^{*}Marginal detection.

NOTE—The last listed epoch (c) gives the model parameters for the combination of all data, excluding epoch 6. Uncertainties are quoted at 68% confidence.

an analogously constructed light curve in the 0.3–9 keV reference band data was also transformed into Fourier space. The cross spectrum was then constructed by cross-correlating the subject bands with the reference band and averaging all segments. The trivial correlation between the subject and reference bands was subtracted from the cross spectrum and the associated uncertainties were calculated using the expressions of Ingram (2019). Similar to the previous section, the resulting cross spectrum was integrated in two geometrically spaced frequency intervals: 1/16–1 Hz and 1–16 Hz. Finally, the frequency-integrated cross spectra were normalized to complex covariance (Uttley et al. 2014; Ingram 2019).

Figure 3 shows the obtained energy dependent covariance in the two selected frequency intervals. The left

panel highlights frequency intervals in comparison to the reference band power spectrum, whereas the other two panels show the fractional amplitude of the complex covariance spectra, and the associated time-lags (calculated as $\tau = \phi/(2\pi\nu)$, where ϕ is the phase angle of the complex covariance, and ν the geometric mean of the frequency band). A few noteworthy properties can be deduced from this figure. First, the covariance pivots as a function of frequency: the faster (hump) component is less covariant below 1 keV and more covariant above 1 keV as compared with the slower (break) component. This indicates that the faster variations have a harder energy spectrum. Second, the time-lag between the subject and reference bands increases with energy. This implies that the stochastic variability is seen in the soft

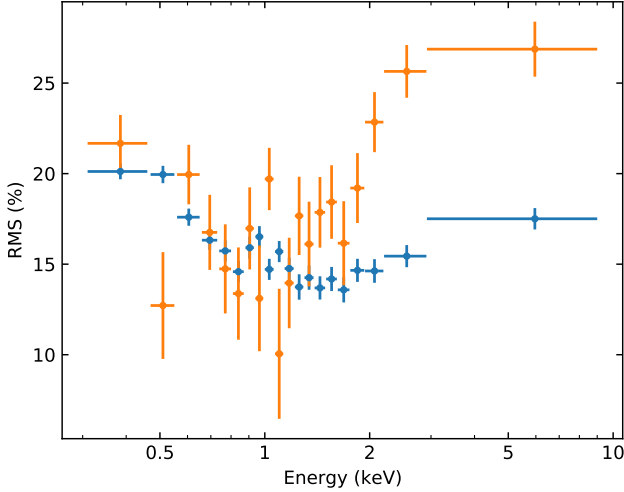


Figure 2. Energy spectrum of the integrated rms in the 1/16 – 1 Hz frequency interval (blue) and the 1 – 16 Hz interval (orange). These intervals were chosen to correspond (roughly) with the break and hump components of the multi-Lorentzian power spectrum model (see Table 2). All error bars show 1σ uncertainties.

band first, and only arrives at harder photon energies at later times. Third, at the highest photon energies both the fractional covariance and the lag turn over and start decreasing. This suggests that the complex covariance is build up from multiple emission components, each intrinsically variable and slightly out of phase.

3.3.1. Complex covariance models

Casting the covariance in units of absolute rms allows the spectrum to be convolved with the instrument response and to be fit with spectral modeling tools. Following Mastroserio et al. (2018), I express the spectral model in the complex plane, and then jointly fit the real and imaginary projections to the data using XSPEC (version 12.11; Arnaud 1996). For spectral models that are time variable in their normalization only, the real line implementations available within XSPEC can be embedded into the complex plane by multiplying them with a factor $e^{i\varphi}$. The real projection of spectrum $s(E)$, with E the photon energy, thus follows trivially as $s(E) \cos \varphi$, and the imaginary part as $s(E) \sin \varphi$. If the parameters shaping the spectral density are time-variable as well, however, then the expected shape of the covariance spectrum will not be the same as the time-averaged version. To illustrate, consider the well explored example of a power law model that has a time-variable photon index (Kotov et al. 2001; Körding & Falcke 2004; Mastroserio et al. 2018). Assuming that the variability is small compared to the time-averaged photon index, one can write $\Gamma(t) = \Gamma_0 + \Gamma_1(t)$, where $\Gamma_1(t) \ll \Gamma_0$. To first order in photon index, the time-dependent energy spectrum can

then be expressed as

$$s_{\text{pl}}(E, t) = a(t) E^{-\Gamma_0} (1 + \Gamma_1(t) \log E), \quad (1)$$

where $a(t)$ is used to encapsulate the time-variability of the normalization. Again following Mastroserio et al. (2018), I can adopt the notation $A(\nu)$ and $B(\nu)$ for the Fourier transforms of the time variable function $a(t)$ and $b(t) = a(t)\Gamma_1(t)$, respectively, the Fourier transformed spectral density becomes

$$S_{\text{pl}}(E, \nu) = A(\nu) E^{-\Gamma_0} + B(\nu) E^{-\Gamma_0} \log E. \quad (2)$$

To construct the complex covariance, one has to multiply the above expression with the complex conjugate of the Fourier transform of the reference band, and then divide by its modulus. The model covariance then takes the form

$$C_{\text{pl}}(E, \nu) = A(\nu) \left[e^{i\varphi_A(\nu)} E^{-\Gamma_0} + \rho(\nu) e^{i\varphi_B(\nu)} e^{-\Gamma_0} \log E \right], \quad (3)$$

where $\varphi_A(\nu)$ and $\varphi_B(\nu)$ give the frequency dependent phase lags between the subject and reference bands associated with the first and second order terms of the Taylor expansion in photon index, and $\rho(\nu) = |B(\nu)|/|A(\nu)|$ gives a correlation factor between these two terms. While one could attempt relate the $\rho(\nu)$ and $\varphi_B(\nu)$ more directly to the variability of the photon index, this would require adopting a physical model for both $a(t)$ and $\Gamma_1(t)$. As noted by Mastroserio et al. (2018), such a model assumption is not actually required for fitting the covariance. Thus, for an integrated frequency range, the complex covariance of a variable power law is a five parameter model that depends on the time-averaged photon index, Γ_0 , and on on four additional Fourier terms: A , ρ , φ_A , and φ_B .

In a similar vein, I can also derive the complex covariance of a blackbody emitter that varies in both normalization and temperature. Consider that the spectral density of blackbody radiation is

$$s_{\text{bb}}(E, t) = a(t) \frac{E^2}{\exp(E/T(t)) - 1}, \quad (4)$$

where $T(t)$ gives the time-variable blackbody temperature in units of energy, and the physical constants have been absorbed into the time-variable normalization $a(t)$. Again, assuming that the variability in temperature is small compared to the time-averaged mean, one can write $T(t) = T_0 + T_1(t)$ with $T_1(t) \ll T_0$. Then, the first order Taylor expansion of the blackbody spectrum

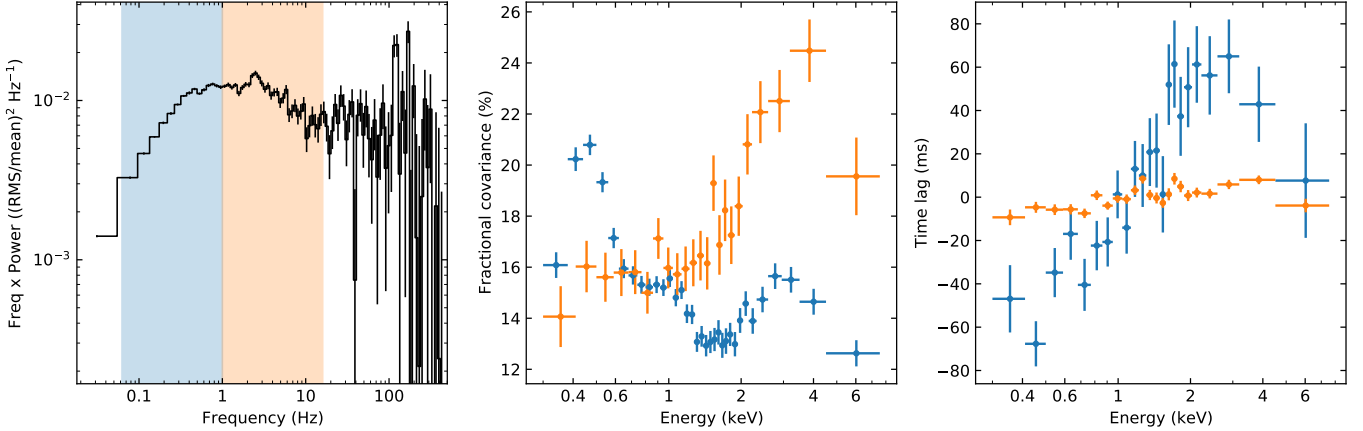


Figure 3. Complex covariance of IGR J17062–6143 in two frequency intervals. The left panel shows the reference band (0.3 – 9 keV) power density spectrum in black, with blue and orange bands highlighting the 1/16 – 1 Hz and 1 – 16 Hz frequency intervals, respectively. The middle panel shows the fractional covariance amplitude for the two frequency intervals as a function of energy. The right panel shows the covariant time-lag associated for the two frequency intervals as a function of energy. All error bars show 1σ uncertainties.

around T_0 is

$$s_{\text{bb}}(E, t) = a(t) \left[\frac{E^2}{\exp(E/T_0) - 1} + T_1(t) \frac{E^3 \exp(E/T_0)}{T_0^2 (\exp(E/T_0) - 1)^2} \right], \quad (5)$$

Through an analogous construction as applied in the previous paragraph, the complex covariance becomes

$$C_{\text{bb}}(E, \nu) = A(\nu) \left[e^{i\varphi_A(\nu)} \frac{E^2}{\exp(E/T_0) - 1} + \rho(\nu) e^{i\varphi_B(\nu)} \frac{E^3 \exp(E/T_0)}{T_0^2 (\exp(E/T_0) - 1)^2} \right], \quad (6)$$

where, for ease of notation, I have recycled the naming convention of the four Fourier terms ($A, \rho, \varphi_A, \varphi_B$). Equations 3 and 6 were implemented as local XSPEC models and have been made publicly available². In the following, I will refer to these models as `covpl` and `covbb`, respectively.

3.4. Spectral fitting

The time-averaged spectrum of IGR J17062 is well-described as an absorbed blackbody and power law, with an additional Gaussian emission line centered at 1 keV (Degenaar et al. 2017; van den Eijnden et al. 2018; Bult et al. 2021a). Adopting the Tübingen-Boulder model for the interstellar absorption (Wilms et al. 2000), the analogous spectrum for the complex covariance can be expressed as

² <https://github.com/peterbult/cov-models>

`tbabs × (complex×gauss + covbb + covpl),`

where `complex` is a simple multiplicative XSPEC model that calculates either the sine or cosine of a joint phase argument, depending on a switch parameter.

Applying the above model without any external constraints produces a reasonable good fit to the complex covariance spectrum of IGR J17062, yielding a best-fit χ^2/dof of 182/122 for the lower frequency interval and 152/122 for the higher frequency interval. The associated best-fit parameters are listed in Table 3.

Compared to the spectral parameters of the time-averaged spectrum, the complex covariance yields a larger mean blackbody temperature (0.6 keV versus 0.4 keV). In an alternative approach, I also fit the covariance spectra jointly with the time-averaged energy spectrum, which allows for the mean blackbody temperature, the power law photon index, and the Gaussian line parameters of the covariance spectra to be tied to their respective counterparts in the time-averaged spectrum. Even with the mean spectral shape constrained, the covariance model is still able to adapt to the data. The total χ^2 of this fit is 584 for 464 degrees of freedom. The specific χ^2 contribution of the lower frequency interval covariance is 188, while the higher frequency interval contributed a χ^2 of 155. Hence, this alternative description of the covariance data is slightly worse, but not significantly so. Figure 5 shows the best-fit model and residuals in the real and imaginary projection, and the detailed best-fit parameters are listed in Table 3.

4. DISCUSSION

I have presented an analysis of the stochastic variability of IGR J17062 using NICER observations. A study of the power density spectrum showed that the aperiodic variability is (mostly) stable with time, showing pronounced band-limited noise as well as several QPOs.

Table 3. Covariance spectrum model parameters

Component	Parameter	Free		Tied	
		break (1/16 – 1 Hz)	hump (1 – 16 Hz)	break (1/16 – 1 Hz)	hump (1 – 16 Hz)
covbb	kT (keV)	$0.61^{+0.06}_{-0.07}$	$0.62^{+0.12}_{-0.04}$		$0.4049^{+0.0026}_{-0.0020}$
	φ_A (deg)	11^{+7}_{-8}	8^{+11}_{-10}	-30 ± 20	-60 ± 30
	φ_B (deg)	179^{+12}_{-16}	160 ± 20	39^{+4}_{-12}	33^{+14}_{-8}
	ρ	$0.10^{+0.04}_{-0.05}$	$0.09^{+0.08}_{-0.03}$	$0.16^{+0.09}_{-0.04}$	0.24 ± 0.10
	K_{bb} (km/10 kpc) ²	2.5 ± 0.7	$4.3^{+0.5}_{-1.7}$	$3.4^{+0.2}_{-1.1}$	4.8 ± 1.4
covpl	Γ	$1.95^{+0.06}_{-0.07}$	$1.73^{+0.30}_{-0.14}$		$1.786^{+0.019}_{-0.007}$
	φ_A (deg)	$-3.8^{+1.8}_{-1.3}$	-10^{+6}_{-3}	$-2.9^{+1.0}_{-0.8}$	$-3.9^{+1.6}_{-3.0}$
	φ_B (deg)	-100^{+140}_{-50}	-160 ± 30	-22^{+7}_{-10}	-159^{+14}_{-9}
	ρ	$0.03^{+0.05}_{-0.03}$	$0.11^{+0.28}_{-0.10}$	$0.126^{+0.020}_{-0.018}$	$0.22^{+0.09}_{-0.06}$
	norm ($\times 10^{-3}$)	$2.19^{+0.09}_{-0.11}$	$2.10^{+0.31}_{-0.13}$	$1.91^{+0.09}_{-0.03}$	$1.90^{+0.16}_{-0.11}$
complex \times	line energy (keV)	$1.002^{+0.013}_{-0.016}$	$0.96^{+0.06}_{-0.04}$		$0.970^{+0.005}_{-0.004}$
	width (keV)	$0.136^{+0.019}_{-0.012}$	$0.15^{+0.02}_{-0.05}$		$0.172^{+0.005}_{-0.008}$
Gaussian	φ_A (deg)	-2^{+8}_{-7}	10^{+10}_{-14}	1^{+2}_{-6}	13^{+12}_{-13}
	norm ($\times 10^{-4}$)	$3.0^{+0.5}_{-0.3}$	$3.2^{+0.5}_{-1.1}$	3.9 ± 0.3	$3.7^{+1.0}_{-0.8}$
χ^2 / dof		182/122	152/122		584/464

NOTE—All phases express the lag with respect to the 0.3 – 9 keV reference band. The absorption column density was set to $N_H = 0.1 \times 10^{22} \text{ cm}^{-2}$ (Bult et al. 2021a). Uncertainties are quoted at 90% confidence.

A spectral analysis of the energy-dependent complex covariance further showed that the band-limited noise can be described with the same blackbody plus power law model explaining the time-averaged energy spectrum when suitably accounting for the time-dependence of the blackbody temperature and power law photon index. In the following I first briefly consider the one epoch that showed a deviating power spectrum, and follow with a discussion of the main results relating to the observed QPOs and the energy-dependent complex covariance analysis of the band-limited noise.

4.1. Epoch 6

All epochs analysed in this paper showed power spectra dominated by broad band-limited noise with $\sim 25\%$ rms below 16 Hz. Such power spectra are typical for (hard) island state accreting neutron stars (van der Klis 2006), and could be well described with two Lorentzian profiles: the break and hump components. For most epochs, the shape of this broad noise was nearly identical, as evident from the tight clustering of the power spectral fit parameters listed in Table 2. Only epoch 6 notably deviates, with break and hump frequencies that are each about a factor two larger than in the other epochs.

It is not at all clear why only epoch 6 deviates from the larger sample. Systematic shifts in the characteristic frequencies are common in low mass X-ray binaries

(Wijnands & van der Klis 1999; Psaltis et al. 1999), but should correlate with spectral hardness or luminosity as the evolution is believed to be driven by a changing mass accretion rate. Considering the position of this one epoch in terms of its count-rate and hardness ratio (Table 1), however, it is clearly not an outlier. Of course the correlated temporal and spectral source state evolution is observed over orders of magnitude changes in characteristic frequencies and source intensity. The observed change in frequencies during epoch 6 are only a factor two, so perhaps the underlying change in the variability mechanism (presumably an increase in mass flow through the disk) was simply not strong enough or sustained for long enough to trigger a similar change in the emission processes.

4.2. Quasi-periodic oscillations

The power spectra of IGR J17062 show two QPOs at low frequencies. The first is centered at 2.6 Hz and was identified as the LF QPO in the variability nomenclature for neutron stars. The QPO is observed in epoch 8 and in the combined power spectrum, although in the latter case the feature is slightly broader. Such broadening is not uncommon when averaging power spectra over many different observational epochs (see, e.g., van Doesburgh & van der Klis 2017, for a discussion), and suggests that the underlying QPO frequency has a modest scatter across the different epochs. The second QPO is centered

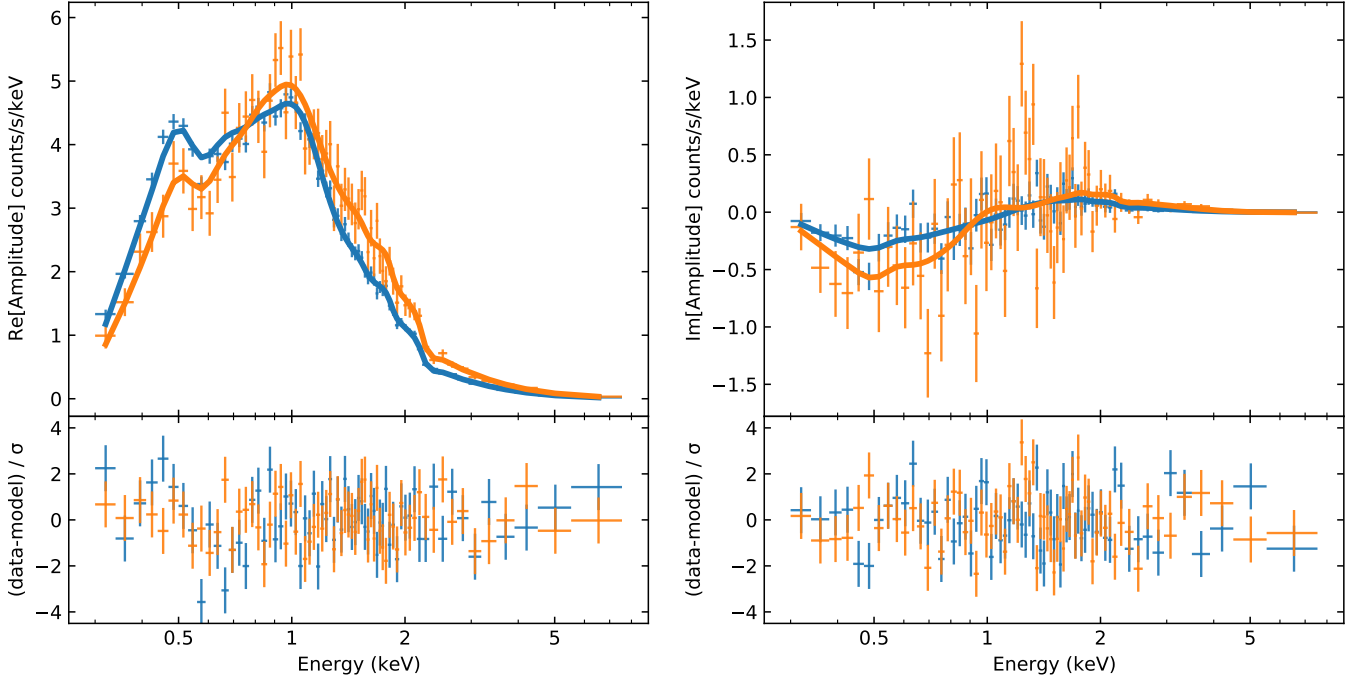


Figure 4. Model fit to the complex covariance in the real (left) and imaginary (right) planes (see Table 3, ‘tied’ model). The top panels show the data and best fit models, while the bottom panels show the residuals divided by the uncertainties. In all panels the blue curve and data show the $1/16 - 1$ Hz frequency interval, while the orange curve and data show the $1 - 16$ Hz interval. All error bars show 1σ uncertainties.

at 5.6 Hz and seen in the combined power spectrum only. The centroid frequency of this second QPO is consistent with being an integer multiple of the LF QPO centroid frequency (at a 2σ level), suggesting that the two QPOs might be harmonically related. Higher harmonics of the LF QPO are again a common feature in the power spectra of neutron stars, especially in the hard state (van Doesburgh & van der Klis 2017). The one aspect of these QPOs that is unusual is their frequency relation with respect to the hump component. In a comprehensive study of LF QPOs across various accreting neutron stars van Doesburgh & van der Klis (2017, 2019) found that the LF QPO frequency is always smaller than that of the hump, while the frequency of the LF second harmonic is about the same as the hump frequency. In contrast, the LF frequencies seen in IGR J17062 are about once and twice the hump frequency, suggesting that either IGR J17062 does not neatly follow the established frequency ratios, or that the observed QPOs are really the second and fourth harmonics.

It has long been recognized that the frequency relation between the neutron star LF QPO and the band-limited noise has a striking commonality with the frequency relations between type C QPOs and band-limited noise observed from black hole binaries (Psaltis et al. 1999; Wijnands & van der Klis 1999). Hence, it is commonly assumed that the two features share a common origin that is independent of the precise nature of the compact object. Studies of the typically much more pronounced

type C QPOs has provided strong evidence that driving mechanism is geometric in nature (Motta et al. 2015; Heil et al. 2015; van den Eijnden et al. 2017). While various models have been proposed to explain these QPOs (see Ingram & Motta 2019, for a detailed review), the most sophisticated model associates the QPO with the solid-body precession of the inner accretion disk (Ingram et al. 2009, 2016). Similar precession should also occur in accreting neutron star binaries, although the extrapolation is not straightforward (Altamirano et al. 2012; Bult & van der Klis 2015b; van Doesburgh & van der Klis 2017), with the stellar oblateness and dynamically relevant magnetosphere introducing additional torques on the disk which may modify or even dominate the net precession frequency (Lai 1999; Morsink & Stella 1999; Shirakawa & Lai 2002).

Another relevant result of type C QPOs is that its second harmonic tends to have a softer spectrum than both the fundamental and time-averaged emission (Axelsson et al. 2014; Axelsson & Done 2016). If this property generalizes to neutron stars, it might explain why NICER, with its comparatively soft passband, would be more sensitive to the higher harmonics of the LF QPO than its fundamental. The limited signal power in the QPO unfortunately prevents a more detailed investigation at this time.

4.3. The high-frequency QPOs

Two QPOs are observed at higher frequencies: a 115 Hz QPO detected in the combined power density spectrum, and a (marginal) 330 Hz QPO seen in epoch 2 only. The fact that these QPOs are the fastest aperiodic features in the power spectrum and have comparatively high quality factors is reminiscent of kilohertz QPOs (van der Klis 2006). Such kHz QPOs can appear as twin peaks, although regularly only the upper or lower term of the pair is visible. A ubiquitous property of these QPOs, however, is that their coherence (i.e. the width of the QPO) increases with luminosity. The sharply pronounced (twin) kHz QPOs are seen at high luminosity, when the source is on the banana branch (i.e. the intermediate to soft state). As luminosities decrease, the QPOs broaden and shift to lower frequencies. In this context, the two high frequency QPOs seen in IGR J17062 do not seem consistent with kHz QPOs. Based on the luminosity, energy spectrum, and the overall shape of the power spectrum, IGR J17062 is firmly in the (hard) island state. Indeed, comparing the frequencies of the break and hump noise components with the frequency relations of other LMXBs (see, e.g., van Doesburgh & van der Klis 2017) implies that IGR J17062 is located at the hardest end of the evolutionary track. In this state, upper kHz QPO is expected to have devolved into incoherent noise, while the lower kHz QPO is either not visible at all, or perhaps responsible for the so-called *low* noise component (Psaltis et al. 1999). So, while the frequencies of the two observed QPOs are at least nominally consistent with kHz QPOs, their observed quality factors are normally only seen at much higher luminosities.

The QPOs do seem to have special frequencies with respect to the known 164 Hz neutron star spin frequency. Specifically, the 115 Hz QPO is within 2σ deviation of a 2:3 frequency ratio relative to spin frequency. The 330 Hz, meanwhile, is centered at twice the spin frequency. Note, though, that the latter QPO is not an artifact of the pulse harmonic: with an rms amplitude of about 14% the QPO is far stronger than the 1.8% rms amplitude of the pulse waveform (Bult et al. 2021a), let alone its second harmonic in isolation. Possibly, then, the rotating magnetosphere is exciting resonance frequencies in disk. In the case of the 115 Hz QPO, this resonance might have become visible only due to the unusual long-term stability of IGR J17062 that allowed for large amounts of data to be averaged. The 330 Hz QPO, seen only in epoch 2, is more difficult to understand, as the higher frequency must exists somewhere in the disk to be excited by a resonance mechanism. The fastest periodicity within the accretion disk should be the orbital frequency at the inner edge of the disk, hence, the simple detection of a 330 Hz QPO would imply that the orbital motion must be at least that fast. Assuming Kepler orbital motion around a canonical 1.4 solar mass neutron star with 10 km radius, this QPO frequency implies an inner disk radius of about 36 km, notably smaller than

the $45 \sim 50$ km derived from an analysis of the long-term accretion torque (Bult et al. 2021a). This discrepancy might imply that the accretion torque modelling was incomplete, or, perhaps more plausibly, indicate that the marginal QPO detection was spurious.

4.4. Spectral timing

The energy-dependent complex covariance was calculated in two integrated frequency intervals that roughly coincide with the break and hump Lorentzian components of the power spectra. These covariance spectra showed systematic hard lags, and fractional amplitudes that become harder as the variability frequency increases. These patterns are qualitatively similar to the hard state covariance spectra of the neutron star system Aql X-1 (Bult et al. 2018) and the black hole binary GX 339-4 (Uttley et al. 2011). The key points noted by these studies are that the softest photon energies (around 0.5 keV) have high fractional variability and lead the correlated variations seen at higher energies. The common interpretation of these results attributes the physical process driving the band-limited noise to mass accretion rate fluctuations that propagate inward through the accretion disk (Lyubarskii 1997). The variability is then observed from the accretion disk first. After some propagation delay, the variability is transferred to Comptonizing medium, so that it is observed at higher photon energies at later times. Interestingly, this model does not readily apply to IGR J17062. Multi-wavelength spectral energy density modelling of IGR J17062 indicates that the accretion disk is visible mainly at longer wavelengths and does not meaningfully contribute to the X-ray spectrum (Hernández Santisteban et al. 2019), hence the leading variability at the softest energies cannot be attributed to thermal disk emission. In an alternate interpretation of the complex covariance spectra of Aql X-1, Bult et al. (2018) suggest that a scenario akin to the QPO model of Miller & Lamb (1992); Lee & Miller (1998) can produce the same spectral-timing characteristics. That is, the electron scattering optical depth of the Comptonizing medium may be modulated stochastically, for instance by propagating mass accretion rate fluctuations. This causes the emergent power law photon index to vary, which can give rise to energy dependent time lags.

Various studies of IGR J17062 have found that the time-averaged energy spectrum can be well described with a simple phenomenological model consisting of an absorbed blackbody component, a power law, and Gaussian emission line centered at 1 keV (Degenaar et al. 2017; van den Eijnden et al. 2018; Bult et al. 2021a). The blackbody component is generally interpreted as emission from the neutron star stellar surface, while the power law indicates the presence of a Compton scattering medium. High resolution spectroscopy has shown that the 1 keV emission consists of a continuum of narrow line features (Degenaar et al. 2017; van den Eijnden et al. 2018).

den et al. 2018), suggesting an origin in a remote disk reflection site, or possibly an outflow. In Section 3.3 I generalized this model to be applicable to the complex covariance spectra, and then applied the model to the observed data. Initially, the model was applied to the covariance data only, allowing all parameter to be freely optimized. A notable result of this fit, however, was a mean blackbody temperature of 0.6 keV, which is hotter than the 0.4 keV seen in the time-averaged emission. This discrepancy suggests that the thermal emission might be a multi-temperature blackbody. The two blackbodies could, for example, be associated a cooler stellar surface and hotter boundary layer. The boundary layer, being fed by the variable mass accretion flow, could naturally produce the observed (thermal) variability. As matter spreads out over the stellar surface it is likely the variability dampens out, such that the brighter surface emission does not show up in the covariance spectrum. A problem with this interpretation, however, is that it is inconsistent with the time-averaged energy spectrum. Adding a secondary blackbody to the spectrum with its temperature fixed to 0.6 keV, the associated normalization is found to be $4 \pm 1 (\text{km}/10 \text{kpc})^2$. Hence, this secondary blackbody would have to be modulated at $\approx 100\%$ rms to explain the covariance, which seems improbable.

In an alternative approach, the complex covariance was also fit jointly with the time-averaged spectrum so that the time-averaged spectral parameters could be tied between them. This approach gave a statistically equivalent description of the covariance spectrum, but has the advantage that it enforces self-consistency. Considering the best-fit parameters obtained with this approach (as listed in Table 3) one sees that: first, the blackbody varies comparatively little, with an amplitude of about 5% rms in its normalization; second, the power law varies by about 23% rms, and appears to be the primary source of the variable emission; third, the Gaussian emission feature varies at 20%, comparable to the power law. The spectral shape of both the blackbody and power law vary as well, but because no specific model for the time-dependence has been assumed, these variations cannot be straightforwardly interpreted in terms of $\Gamma(t)$ or $T(t)$. Instead, the fit parameters indicate how much of the fractional rms in the covariance spectrum is contributed by the shape variations, which is 1% for the blackbody temperature, and 5% for the power law photon index. Due to the variable shape of the covariance components, the phase parameters are similarly difficult to interpret directly. A more approachable way to inspect the phases is to decompose the model into its additive components and visualize them in polar coordinates, as shown in Figure 5. This decomposition directly shows how the phase lags of the individual components depend on photon energy, and demonstrate that the variability of both the blackbody

and the Gaussian emission feature lag behind the power law.

Before trying to interpret the spectral fit results in physical terms, it is important to remember the limitations of the phenomenological spectral model. Unlike the simple power law model, the emission spectrum of a Compton scattering medium should roll off at low photon energies (Shapiro et al. 1976; Sunyaev & Titarchuk 1980). Considering the time-averaged spectral model shown in Figure 5 (left panel), it should be clear that the power law is the dominant spectral component below about 1 keV. Hence, relative to a Compton scattering spectrum there is an excess of soft flux. A natural explanation for this soft excess is that it is caused by a disk reflection (see Keek et al. (2017) and Bult et al. (2021b) for disk reflection modelling of IGR J17062). In this sense, the phenomenological model still makes sense if the bulk of the reflection emission originates from close to the neutron star. The observed time lags intrinsic to the power law emission are then much larger than the crossing time delays of the reflection, so that the low energy region, where the reflection dominates the total emission, should closely track the variability of the power law.

Presuming that the phenomenological fit (as shown in Figure 5) is indeed a reasonable approximation to the physical process, the fit results seem well matched by an oscillating Compton scattering medium (Miller & Lamb 1992; Lee & Miller 1998), as proposed for Aql X-1. The power law component clearly dominates the observed variability in IGR J17062 across photon energies, and its pivoting photon index induces the observed hard lags. The lag between the Gaussian line and the power law is easy to understand, as the line feature has been proposed to originate in an outflow or from a distant disk reflection site. In either case the line will be excited by the illuminating power law emission, but have a longer light travel path. So, light travel time delays are naturally expected for this line. The lag between the thermal blackbody emission and the power law can also be explained through one of two scenarios. First, if the electron scattering optical depth is modulated by propagating mass accretion rate fluctuations, then these fluctuations might simply be affecting the Compton scattering medium before they propagate down to the stellar surface. Hence, the time delay between the power law and blackbody variability could simply be a propagation delay. Second, as proposed in more recent theoretical implementations of the variable Compton scattering model (Kumar & Misra 2014; Karpouzas et al. 2020), the power law emission of Compton scattering medium should also illuminate the disk and star giving rise to a radiative feedback mechanism between the star/disk and the Compton scattering region. Hence, the delayed (and reduced) variability observed in the blackbody might be induced by the X-ray heating of the stellar surface by the non-thermal emission. Qualitatively, this scenario

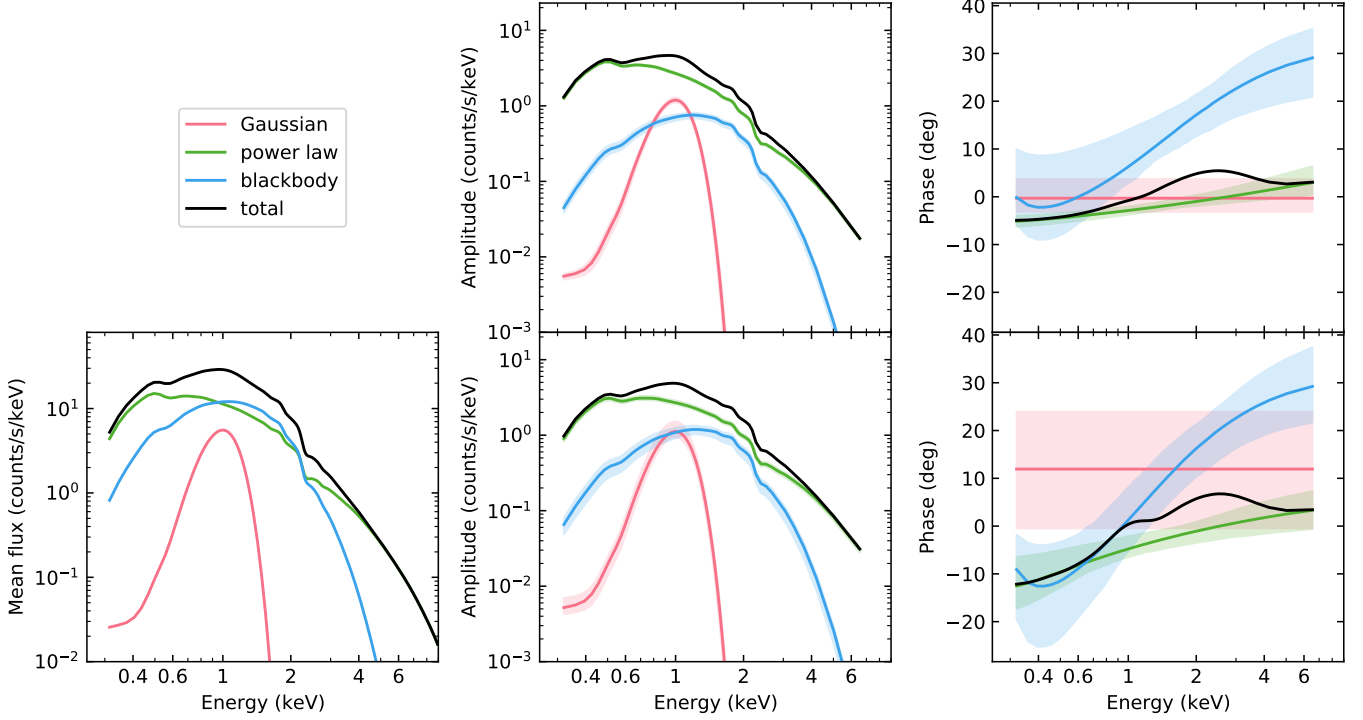


Figure 5. Decomposition of the (folded) complex covariance model (see Table 3, ‘tied’ model). The left panel shows the time-averaged energy spectrum of IGR J17062. The middle column shows the amplitude of the complex covariance model, while the right column shows the phase. The top and bottom rows show the $1/16 - 1$ Hz and $1 - 16$ Hz intervals, respectively. In all panels the black line shows the best-fit total model, whereas the red, green, and light blue lines show the respective contributions from the 1 keV Gaussian line, the power law, and the blackbody. The shaded areas show the 90% confidence region associated with each spectral component.

appears to fit well the spectral modelling of the covariance spectrum in IGR J17062. The next question, then, would be if the model of Kumar & Misra (2014) and Karpouzas et al. (2020), which is developed for QPOs, is able to account for the band-limited noise as well, and if the predictions of that model can quantitatively match the measured covariance spectra of IGR J17062. Given that the aim of this paper was to report on stochastic variability of IGR J17062, this more detailed modelling effort is left for future work.

5. SUMMARY

In summary, I have presented an analysis of the stochastic X-ray variability of the accreting millisecond X-ray pulsar IGR J17062. Over the course of three years of monitoring, the power density spectra of this source have remained mostly stable, showing broad band-limited noise at low frequencies, as is typical for hard state neutron star LMXBs. By combining these

data I have found evidence for a relative common low-frequency QPO as well as an unusual 115 Hz QPO that may be due to a 2:3 resonance with the stellar spin frequency. Further, a spectroscopic study of the complex covariance showed that the continuum noise can be qualitatively explained as being due to a time variable Compton-scattering medium, in which the variability observed in the emission feature and at the lowest photon energies are attributed to the disk reflection of the power law continuum.

Facilities: ADS, HEASARC, NICER

Software: heasoft (v6.27.2), nicerdas (v7a)

This work was supported by NASA through the Astrophysics Data Analysis Program (grant number 80NSSC20K0288) and the CRESST II cooperative agreement (80GSFC21M0002), and made use of data and software provided by the High Energy Astrophysics Science Archive Research Center (HEASARC).

REFERENCES

Altamirano, D., Ingram, A., van der Klis, M., et al. 2012, *ApJL*, 759, L20
 Altamirano, D., van der Klis, M., Méndez, M., et al. 2008, *ApJ*, 685, 436

Arnaud, K. A. 1996, in Astronomical Society of the Pacific Conference Series, Vol. 101, Astronomical Data Analysis Software and Systems V, ed. G. H. Jacoby & J. Barnes, 17

Axelsson, M., & Done, C. 2016, *MNRAS*, 458, 1778

Axelsson, M., Done, C., & Hjalmarsdotter, L. 2014, *MNRAS*, 438, 657

Belloni, T., Psaltis, D., & van der Klis, M. 2002, *ApJ*, 572, 392

Bildsten, L. 1998, *ApJL*, 501, L89

Bult, P., Strohmayer, T. E., Malacaria, C., Ng, M., & Wadiasingh, Z. 2021a, *ApJ*, 912, 120

Bult, P., & van der Klis, M. 2015a, *ApJL*, 798, L29

Bult, P., & van der Klis, M. 2015b, *ApJ*, 806, 90

Bult, P., van Doesburgh, M., & van der Klis, M. 2017, *ApJ*, 845, 124

Bult, P., Arzoumanian, Z., Cackett, E. M., et al. 2018, *ApJL*, 859, L1

Bult, P., Altamirano, D., Arzoumanian, Z., et al. 2021b, *arXiv e-prints*, arXiv:2107.13543

Chakrabarty, D., Morgan, E. H., Munro, M. P., et al. 2003, *Nature*, 424, 42

Churazov, E., Sunyaev, R., Revnivtsev, M., et al. 2007, *A&A*, 467, 529

Degenaar, N., Miller, J. M., Wijnands, R., Altamirano, D., & Fabian, A. C. 2013, *ApJL*, 767, L37

Degenaar, N., Pinto, C., Miller, J. M., et al. 2017, *MNRAS*, 464, 398

Di Salvo, T., & Sanna, A. 2020, *arXiv e-prints*, arXiv:2010.09005

Folkner, W. M., Williams, J. G., Boggs, D. H., Park, R. S., & Kuchynka, P. 2014, *Interplanetary Network Progress Report*, 42-196, 1

Gendreau, K., & Arzoumanian, Z. 2017, *Nature Astronomy*, 1, 895

Hasinger, G., & van der Klis, M. 1989, *A&A*, 225, 79

Heil, L. M., Uttley, P., & Klein-Wolt, M. 2015, *MNRAS*, 448, 3348

Hernández Santisteban, J. V., Cúneo, V., Degenaar, N., et al. 2019, *MNRAS*, 488, 4596

in 't Zand, J. J. M., Verbunt, F., Strohmayer, T. E., et al. 1999, *A&A*, 345, 100

Ingram, A. 2019, *MNRAS*, 489, 3927

Ingram, A., Done, C., & Fragile, P. C. 2009, *MNRAS*, 397, L101

Ingram, A., van der Klis, M., Middleton, M., et al. 2016, *MNRAS*, 461, 1967

Ingram, A. R., & Motta, S. E. 2019, *NewAR*, 85, 101524

Karpouzas, K., Méndez, M., Ribeiro, E. M., et al. 2020, *MNRAS*, 492, 1399

Keek, L., Iwakiri, W., Serino, M., et al. 2017, *ApJ*, 836, 111

Körding, E., & Falcke, H. 2004, *A&A*, 414, 795

Kotov, O., Churazov, E., & Gilfanov, M. 2001, *MNRAS*, 327, 799

Kumar, N., & Misra, R. 2014, *MNRAS*, 445, 2818

Lai, D. 1999, *ApJ*, 524, 1030

Leahy, D. A., Elsner, R. F., & Weisskopf, M. C. 1983, *ApJ*, 272, 256

Leahy, D. A., Morsink, S. M., & Cadeau, C. 2008, *ApJ*, 672, 1119

Lee, H. C., & Miller, G. S. 1998, *MNRAS*, 299, 479

Lyubarskii, Y. E. 1997, *MNRAS*, 292, 679

Mastroserio, G., Ingram, A., & van der Klis, M. 2018, *MNRAS*, 475, 4027

Miller, G. S., & Lamb, F. K. 1992, *ApJ*, 388, 541

Morsink, S. M., & Stella, L. 1999, *ApJ*, 513, 827

Motta, S. E., Casella, P., Henze, M., et al. 2015, *MNRAS*, 447, 2059

Negoro, H., Serino, M., Sasaki, R., et al. 2015, *The Astronomer's Telegram*, 8241, 1

Nelson, L. A., & Rappaport, S. 2003, *ApJ*, 598, 431

Nishida, H., Serino, M., Iwakiri, W., et al. 2020, *The Astronomer's Telegram*, 13827, 1

Poutanen, J., & Gierliński, M. 2003, *MNRAS*, 343, 1301

Psaltis, D., Belloni, T., & van der Klis, M. 1999, *ApJ*, 520, 262

Psaltis, D., & Chakrabarty, D. 1999, *ApJ*, 521, 332

Psaltis, D., Öznel, F., & Chakrabarty, D. 2014, *ApJ*, 787, 136

Ricci, C., Beckmann, V., Carmona, A., & Weidenspointner, G. 2008, *The Astronomer's Telegram*, 1840, 1

Shapiro, S. L., Lightman, A. P., & Eardley, D. M. 1976, *ApJ*, 204, 187

Shirakawa, A., & Lai, D. 2002, *ApJ*, 564, 361

Strohmayer, T. E., Arzoumanian, Z., Bogdanov, S., et al. 2018, *ApJL*, 858, L13

Sunyaev, R. A., & Titarchuk, L. G. 1980, *A&A*, 500, 167

Uttley, P., Cackett, E. M., Fabian, A. C., Kara, E., & Wilkins, D. R. 2014, *A&A Rev*, 22, 72

Uttley, P., Wilkinson, T., Cassatella, P., et al. 2011, *MNRAS*, 414, L60

van den Eijnden, J., Ingram, A., Uttley, P., et al. 2017, *MNRAS*, 464, 2643

van den Eijnden, J., Degenaar, N., Pinto, C., et al. 2018, *MNRAS*, 475, 2027

van der Klis, M. 2006, in *Compact stellar X-ray sources*, ed. W. H. G. Lewin & M. van der Klis (Cambridge: Cambridge University Press), 39–112

van Doesburgh, M., & van der Klis, M. 2017, *MNRAS*, 465, 3581

van Doesburgh, M., & van der Klis, M. 2019, *MNRAS*, **490**, 5270

van Straaten, S., van der Klis, M., & Méndez, M. 2003, *ApJ*, **596**, 1155

van Straaten, S., van der Klis, M., & Wijnands, R. 2005, *ApJ*, **619**, 455

Wijnands, R., & van der Klis, M. 1998, *ApJL*, **507**, L63

Wijnands, R., & van der Klis, M. 1999, *ApJ*, **514**, 939

Wijnands, R., van der Klis, M., Homan, J., et al. 2003, *Nature*, **424**, 44

Wilms, J., Allen, A., & McCray, R. 2000, *ApJ*, **542**, 914